

Northumbria Research Link

Citation: Zhang, Jingao, Yuan, Jinhui, Qu, Yuwei, Qiu, Shi, Mei, Chao, Zhou, Xian, Yan, Binbin, Wu, Qiang, Wang, Kuiru, Sang, Xinzhu and Yu, Chongxiu (2022) A novel surface plasmon resonance-based photonic crystal fiber refractive index sensor with an ultra-wide detection range. *Optik*, 259. p. 168977. ISSN 0030-4026

Published by: Elsevier

URL: <https://doi.org/10.1016/j.ijleo.2022.168977>
<<https://doi.org/10.1016/j.ijleo.2022.168977>>

This version was downloaded from Northumbria Research Link:
<https://nrl.northumbria.ac.uk/id/eprint/48883/>

Northumbria University has developed Northumbria Research Link (NRL) to enable users to access the University's research output. Copyright © and moral rights for items on NRL are retained by the individual author(s) and/or other copyright owners. Single copies of full items can be reproduced, displayed or performed, and given to third parties in any format or medium for personal research or study, educational, or not-for-profit purposes without prior permission or charge, provided the authors, title and full bibliographic details are given, as well as a hyperlink and/or URL to the original metadata page. The content must not be changed in any way. Full items must not be sold commercially in any format or medium without formal permission of the copyright holder. The full policy is available online: <http://nrl.northumbria.ac.uk/policies.html>

This document may differ from the final, published version of the research and has been made available online in accordance with publisher policies. To read and/or cite from the published version of the research, please visit the publisher's website (a subscription may be required.)

A novel surface plasmon resonance-based photonic crystal fiber refractive index sensor with an ultra-wide detection range

Jingao Zhang¹, Jinhui Yuan^{1,2,*}, Yuwei Qu¹, Shi Qiu¹, Chao Mei², Xian Zhou², Binbin Yan¹,
Qiang Wu³, Kuiru Wang^{1,*}, Xinzhu Sang¹, and Chongxiu Yu¹

¹State Key Laboratory of Information Photonics and Optical Communications,
Beijing University of Posts and Telecommunications, Beijing 100876, China

²Research Center for Convergence Networks and Ubiquitous Services,
University of Science & Technology Beijing (USTB), Beijing 100083, China

³Department of Physics and Electrical Engineering, Northumbria University,
Newcastle upon Tyne, NE1 8ST, United Kingdom

*Corresponding authors: yuanjinhui81@bupt.edu.cn; krwang@bupt.edu.cn

Abstract: In this paper, a novel photonic crystal fiber (PCF) refractive index (RI) sensor with an ultra-wide detection range based on the surface plasmon resonance (SPR) effect is proposed. By selectively filling the air hole with the analyte and introducing the gold-coated air hole, the high performance RI sensing can be achieved. The simulation results show that the asymmetric structure of the PCF makes the x -polarization (x -pol) and y -polarization (y -pol) core modes have different sensing characteristics. The average wavelength sensitivity of the proposed SPR-PCF RI sensor can reach -4523 nm/RIU in the RI range from 1.25 to 1.45 for the x -pol core mode as well as -4851 nm/RIU in the RI range from 1.25 to 1.49 for the y -pol core mode. The maximum amplitude sensitivities of -1239.19 RIU⁻¹ and -1633.54 RIU⁻¹ for the x -pol and y -pol core modes are also achieved. Moreover, the proposed SPR-PCF RI sensor can obtain the maximum resolutions of 1.603×10^{-5} and 1.695×10^{-5} RIU and figure of merits of 226.92 and 105.76 RIU⁻¹ for the x -pol and y -pol core modes, respectively. It is believed that the proposed SPR-PCF RI sensor has potential applications in the chemistry, biology, and environment monitoring.

Keywords: Photonic crystal fiber, surface plasmon resonance, refractive index sensor, ultra-wide detection range.

1. Introduction

Surface plasmon resonance (SPR)-based sensors have attracted more attentions in recent years due to their excellent sensing performances and wide range of application scenarios [1-6]. The SPR effect refers to a phenomenon caused by the collective electronic vibration. When the phase-matching conditions are satisfied, the energy of the incident light is coupled with the surface plasmon wave (SPW), resulting in a sharp increase in the confinement loss of the light field at the resonant wavelength [7-9]. The excellent structural controllability and optical characteristics of the photonic crystal fibers (PCFs) make the SPR based PCFs have great potential in the biomedical and chemical sensing, especially in the refractive index (RI) sensing [10-13]. In 2006, Hassani et al firstly proposed highly sensitive SPR-PCF sensor [14]. Since then, the SPR-PCF RI sensor has gradually become a research hotspot.

As the PCF design and fabrication technologies develop, some SPR-PCF RI sensors have been proposed. In 2015, Rifat et al. reported a SPR-PCF sensor with selective analyte channels and

graphene-silver deposited core for RI sensing [15]. In 2018, Hasan et al. proposed a SPR RI sensor based on dual-polarized spiral PCF coated with the gold in the RI range of 1.33-1.38, and the proposed SPR-PCF sensor could realize different sensitivities for the x -pol and y -pol modes [16]. In 2019, Pathak et al. designed a concave-shaped SPR-PCF RI sensor covered with the multiple gold nanowires, where the wavelength sensitivity (WS) of 4471 nm/RIU and amplitude sensitivity (AS) of 214 RIU⁻¹ in the RI range from 1.33 to 1.38 were achieved [17]. In 2019, Chen et al. designed a dual optofluidic channel SPR-PCF RI sensor, where the WS of 5500 nm/RIU and AS of 150 RIU⁻¹ in the RI range of 1.33 to 1.38 were achieved [18]. In 2021, Yang et al. reported a graphene-Au coated SPR-PCF RI sensor, and the simulation results showed that the maximum WS and AS were 4200 nm/RIU and 450 RIU⁻¹ in the RI range of 1.32 to 1.41, respectively [19]. From the previous works, it is possible to design a SPR-PCF RI sensor with high sensitivity and wide detection range.

In this paper, we propose a novel SPR-PCF RI sensor with an ultra-wide detection range. The propagation characteristics and effects of the structure parameters of the proposed SPR-PCF RI sensor are investigated by using the finite element method (FEM). By coating the gold film on an air hole and introducing the birefringence in the cladding structure, the excellent sensing performances of the proposed SPR-PCF RI sensor can be achieved. It is demonstrated that for the proposed SPR-PCF RI sensor, the average WS can reach -4523 nm/RIU in the RI range from 1.25 to 1.45 for the x -pol core mode as well as -4851 nm/RIU in the RI range from 1.25 to 1.49 for the y -pol core mode, and the maximum ASs of -1239.19 RIU⁻¹ and -1633.54 RIU⁻¹ for the x -pol and y -pol core modes can be also achieved, along with the maximum resolutions of 1.603×10^{-5} RIU and 1.695×10^{-5} RIU and figure of merits of 226.92 RIU⁻¹ and 105.76 RIU⁻¹ for the x -pol and y -pol core modes, respectively.

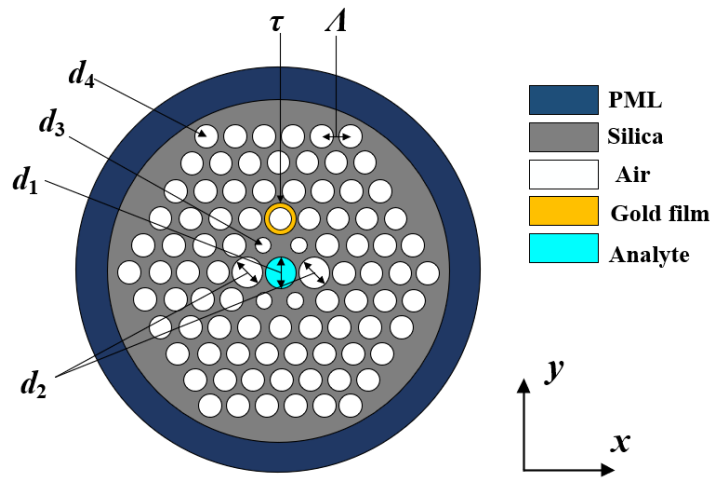


Fig. 1. The cross-sectional structure of the proposed SPR-PCF RI sensor.

Fig. 1 shows the cross-sectional structure of the proposed SPR-PCF RI sensor, From Fig. 1, the structure has five layers of air holes arranged in a triangular lattice with the lattice spacing of A . The central hole is used to fill the measured analyte, and the other holes are filled with air. The birefringence is introduced by changing the air hole sizes in the first layer [20-22]. The diameter of the central air hole is d_1 , the diameters of the air holes in the first layer along the x -axis and y -axis directions are d_2 and d_3 , respectively, and the diameter of the other air holes is d_4 . The thickness of the gold film coated on the central air hole is τ . The initial structural parameters of the SPR-PCF RI sensor are set as following: $d_1=d_2=d_3=d_4=1.4 \mu\text{m}$, $\tau=50 \text{ nm}$, and $A=2 \mu\text{m}$. In the simulation, the FEM is employed, and the fused silica is used as the background material, whose refractive index is

n_{silica} . In order to absorb the radiation energy, we place a perfectly matched layer (PML) around the outer wall of the PCF, and its thickness and refractive index are set as 5 μm and $n_{\text{silica}}+0.03$, respectively [23].

n_{silica} can be obtained by the following Sellmeier equation[24]

$$n_{\text{silica}}(\lambda) = \sqrt{1 + \frac{0.6961663\lambda^2}{\lambda^2 - (0.00684043)^2} + \frac{0.4079426\lambda^2}{\lambda^2 - (0.1162414)^2} + \frac{0.897479\lambda^2}{\lambda^2 - (9.896161)^2}}, \quad (1)$$

where λ is the free-space wavelength.

The dielectric constant of the gold material can be calculated by the following Drude-Lorentz model [25,26]

$$\varepsilon_m = \varepsilon_\infty - \frac{\omega_D^2}{\omega(\omega - j\gamma_D)} - \frac{\Delta\varepsilon \cdot \Omega_L^2}{(\omega^2 - \Omega_L^2) - j\Gamma_L\omega}, \quad (2)$$

where $\varepsilon_\infty=5.9673$ represents for the permittivity of high frequency and $\Delta\varepsilon=1.09$ represents for the weighting factor. ω is the angular frequency of the guided light, ω_D and γ_D are the plasmon frequency and damping frequency, and Ω_L and Γ_L represent for the frequency and spectral width of the Lorentz oscillator ($\Omega_L/2\pi = 650.07$ THz, $\Gamma_L/2\pi = 104.86$ THz), respectively.

The propagation loss can be characterized by the confinement loss (CL), which can be obtained by following equation [27-30]

$$CL(\text{dB/m}) = \frac{20}{\ln 10} \times k_0 \times \text{Im}(n_{\text{eff}}) \times 10^6, \quad (3)$$

where k_0 is the free space wave number and n_{eff} is the complex effective refractive index of the core mode.

Generally, the WS and AS are usually considered as the two important parameters to measure the sensing performances. The WS and AS can be expressed as following [31-33]

$$\text{WS (nm/RIU)} = \frac{\Delta\lambda_{\text{peak}}}{\Delta n_a}, \quad (4)$$

$$\text{AS (RIU}^{-1}\text{)} = \frac{1}{CL(\lambda, n_a)} \frac{\partial CL(\lambda, n_a)}{\partial n_a}, \quad (5)$$

where $\Delta\lambda_{\text{peak}}$ and Δn_a denotes the variations of the resonant wavelength and the analyte RI, respectively. $CL(\lambda, n_a)$ is the confinement loss at the particular value of the analyte RI, and $\partial CL(\lambda, n_a)$ is the loss difference between the two consecutive RIs.

The resolution (R) and figure of merits (FOM) are used to comprehensively evaluate the sensing performance of the proposed SPR-PCF RI, and can be described as [34-36]

$$R(\text{RIU}) = \frac{\Delta n_a \cdot \Delta\lambda_{\text{min}}}{\Delta\lambda_{\text{peak}}}, \quad (6)$$

$$FOM(\text{RIU}^{-1}) = \frac{\text{WS}}{FWHM}, \quad (7)$$

where $\Delta\lambda_{\text{min}}$ denotes the wavelength resolution of the detector which is set as 0.1 nm, and $FWHM$ is the full-width at half-maximum of the CL peak.

2. Influences of the structure parameters of the SPR-PCF on the propagation characteristics

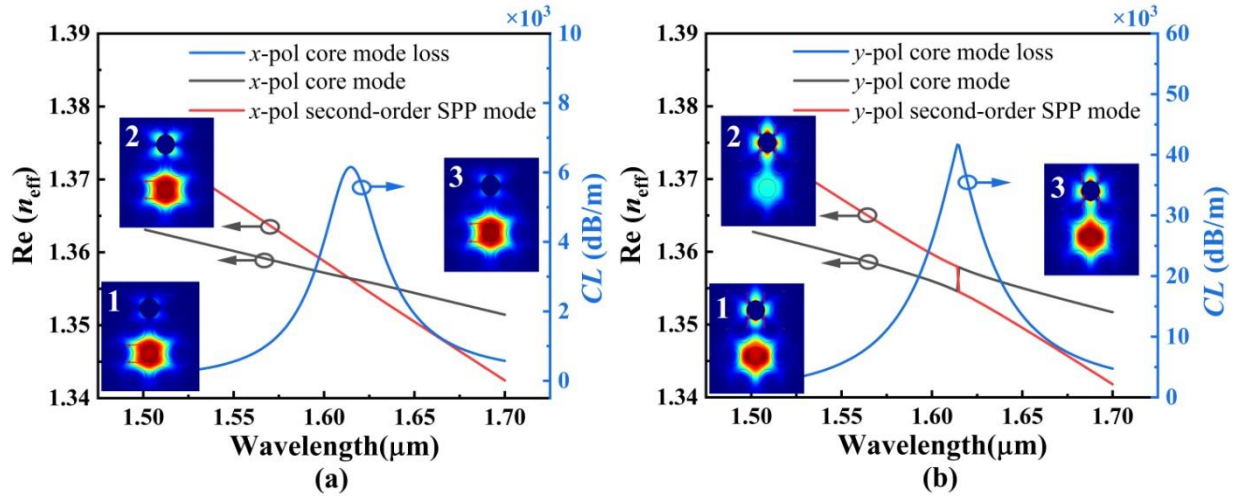


Fig. 2. (a) The effective RI real parts of the x -pol core mode and second-order SPP mode, and the CL spectra of the x -pol core mode when the analyte RI is chosen as 1.35. (b) The effective RI real parts of the y -pol core mode and second-order SPP mode, and the CL spectra of the y -pol core mode when the analyte RI is chosen as 1.35. The inserts 1, 2, and 3 in (a) and (b) show the electric field distributions of the x -pol and y -pol core modes and second-order SPP modes of the proposed SPR-PCF calculated at wavelengths 1.57, 1.615, and 1.66 μm , respectively.

Figs. 2(a) and 2(b) show the effective RI real parts of the x -pol and y -pol core modes and second-order SPP modes, and the CL spectra of the x -pol and y -pol core modes when the initial structural parameters of the SPR-PCF are used and the analyte RI is chosen as 1.35. From Fig. 2(a) when the phase-matching condition is satisfied at wavelength 1.615 μm , the effective RI real part of the x -pol core mode is equal to that of the x -pol second-order surface plasmon polariton (SPP) mode, and the corresponding CL spectrum of the x -pol core mode reaches the peak value. Similarly, it can also be seen from Fig. 2(b) that the effective RI real part of the y -pol core mode is equal to that of the y -pol second-order SPP mode, and the corresponding CL spectrum of the y -pol core mode reaches the peak value at resonant wavelength 1.615 μm . The insets 1, 2, and 3 in Figs. 2(a) and 2(b) show the electric field distributions of the x -pol and y -pol core modes and second-order SPP modes calculated at wavelengths 1.57, 1.615, and 1.66 μm , respectively. It can be seen from the insets 1, 2, and 3 in Figs. 2(a) and 2(b) that for the x -pol and y -pol core modes and second-order SPP modes, the mutual energy coupling between them emerges at the considered three wavelengths, and the complete energy coupling occurs at resonant wavelength 1.615 μm . When the analyte RI changes, the effective RI real part of the x -pol and y -pol second-order SPP modes are obviously affected, so the resonant wavelength occurs to shift. Thus, the RI sensing can be achieved by detecting the change of the resonant wavelength.

In the following, we will investigate the influences of the structure parameters (d_1 , d_2 , d_3 , d_4 , and τ) of the proposed SPR-PCF on the propagation characteristics when the analyte RI is chosen as 1.30, 1.35, and 1.40, respectively. For the proposed SPR-PCF, the structure parameters have great influences on the propagation characteristics, especially the central analyte-filled hole size and the first layer of air hole sizes [37-39]. Figs. 3(a) and 3(b) show the CL spectra of the x -pol and y -pol core modes of the SPR-PCF when d_1 and the analyte RI are changed. The insert in Fig. 3(a) shows

the zoom-in spectra of the x -pol core mode when d_1 is increased from 1.4 to 1.8 μm and the analyte RI is chosen as 1.40. From Fig. 3(a) and the insert, when d_1 is increased from 1.4 to 1.6, and to 1.8 μm and the analyte RI is chosen as 1.30, 1.35, or 1.40, the resonant wavelengths of the x -pol core mode are located at 1757, 1875, and 1992 nm, 1615, 1697, and 1778 nm, and 1449, 1493, and 1572 nm respectively. From Fig. 3(b), when d_1 is increased from 1.4 to 1.6, and 1.8 μm and the analyte RI is chosen as 1.30, 1.35, or 1.40, the resonant wavelengths of the y -pol core mode are located at 1760, 1881, and 2003 nm, 1614, 1698, and 1780 nm, and 1447, 1488, and 1528 nm, respectively. It is found from Figs. 3(a) and 3(b) that with the increase of d_1 , the resonant wavelengths of the x -pol and y -pol core modes occur to red-shift. According to Eq. (4), for the same analyte RI interval, the sensing sensitivity increases with the increase of d_1 both in the x -pol and y -pol core modes. The CL peak value increases for the analyte RI lower than 1.35 but decreases for the analyte RI higher than 1.35. The main reason is considered that with the increase of the analyte RI, it is close to the RI of the silica material, so the coupling strengths between the x -pol and y -pol core modes and second-order SPP mode becomes weaker.

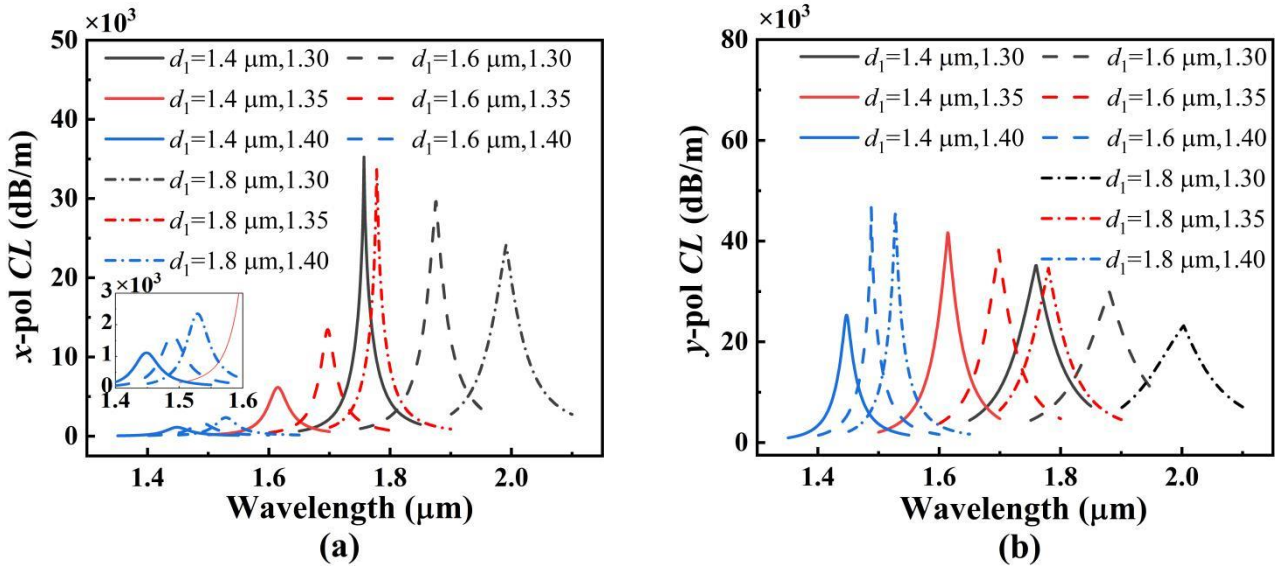


Fig. 3. The CL spectra of the x -pol (a) and y -pol (b) core modes when d_1 is increased from 1.4 to 1.6, and to 1.8 μm and the analyte RI is chosen as 1.30, 1.35, or 1.40, respectively. The insert in (a) shows the zoom-in-spectra of the x -pol core mode when d_1 is increased from 1.4 to 1.8 μm and the analyte RI is chosen as 1.40.

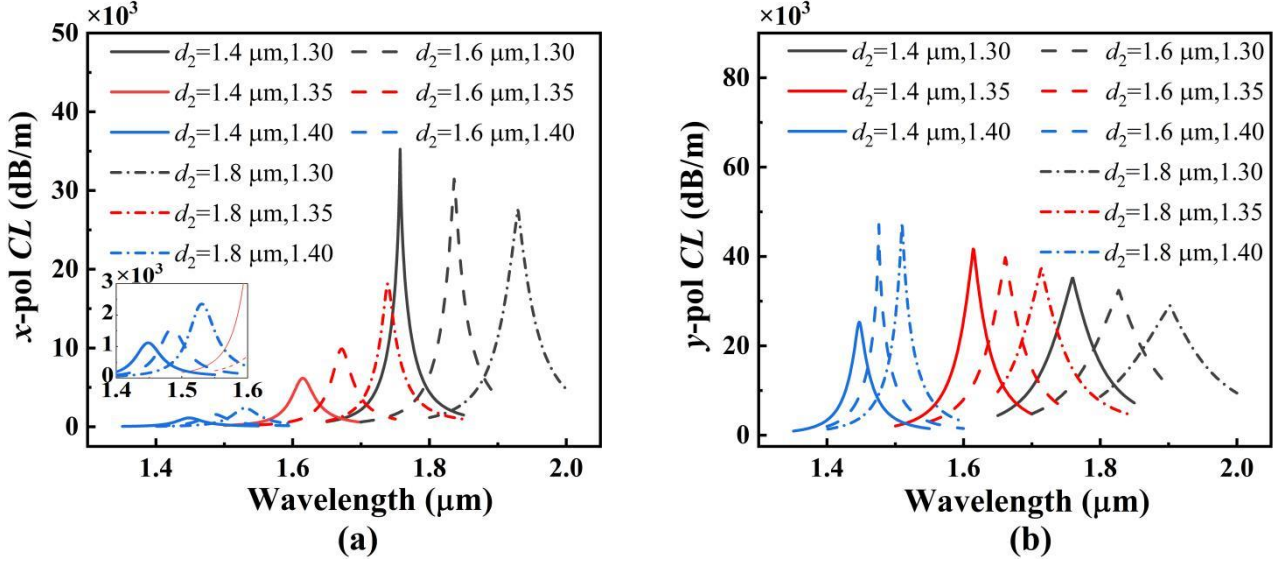


Fig. 4. The *CL* spectra of the *x*-pol (a) and *y*-pol (b) core modes when d_2 is increased from 1.4 to 1.6, and to 1.8 μm and the analyte RI is chosen as 1.30, 1.35, or 1.40, respectively. The insert in (a) shows the zoom-in-spectra of the *x*-pol core mode when d_2 is increased from 1.4 to 1.8 μm and the analyte RI is chosen as 1.40.

Figs. 4(a) and 4(b) show the *CL* spectra of the *x*-pol and *y*-pol core modes of the SPR-PCF when d_2 and the analyte RI are changed. The insert in Fig. 4(a) show the zoom-in-spectra of the *x*-pol core mode when d_2 is increased from 1.4 to 1.8 μm and the analyte RI is chosen as 1.40. From Fig. 4(a) and the insert, when d_2 is increased from 1.4 to 1.6, and to 1.8 μm and the analyte RI is chosen as 1.30, 1.35, or 1.40, the resonant wavelengths of the *x*-pol core mode are located at 1757, 1836, and 1929 nm, 1615, 1672, and 1739 nm, and 1449, 1489, and 1529 nm, respectively. From Fig. 4(b), when d_2 is increased from 1.4 to 1.6, and to 1.8 μm and the analyte RI is chosen as 1.30, 1.35, or 1.40, the resonant wavelengths of the *y*-pol core mode are located at 1760, 1881, and 2003 nm, 1614, 1661, and 1714 nm, and 1447, 1476, and 1510 nm, respectively. From Figs. 4(a) and 4(b), as d_2 is increased, the resonant wavelengths of the *x*-pol and *y*-pol core modes occur to red-shift, and the corresponding sensing sensitivities are enhanced. The main reason is that with the increase of d_2 , the two larger air holes break the symmetry of the SPR-PCF and introduce the birefringence in the *x*-axis direction, thus resulting in different sensitivities of the *x*-pol and *y*-pol core modes. In addition, the *CL* peak value for the analyte RI lower than 1.35 can be obviously increased as d_2 is increased. This may be because the energy leakage in the *x*-axis direction is prevented with the increase of d_2 , which promotes the energy coupling between the *y*-pol core mode and second-order SPP mode.

Figs. 5(a) and 5(b) show the *CL* spectra of the *x*-pol and *y*-pol core modes of the SPR-PCF when d_3 and the analyte RI are changed. The insert in Fig. 5(a) shows the zoom-in-spectra of the *x*-pol core mode when d_3 is increased from 1.2 to 1.6 μm and the analyte RI is chosen as 1.40. From Fig. 5(a) and the insert, when d_3 is increased from 1.2 to 1.4, and to 1.6 μm and the analyte RI is chosen as 1.30, 1.35, or 1.40, the resonant wavelengths of the *x*-pol core mode are located at 1709, 1757, and 1787 nm, 1565, 1615, and 1654 nm, and 1441, 1449, and 1446 nm, respectively. From Fig. 5(b), when d_3 is increased from 1.2 to 1.4, and to 1.6 μm and the analyte RI is chosen as 1.30, 1.35, or 1.40, the resonant wavelengths of the *y*-pol core mode are located at 1690, 1760, and 1821 nm, 1587, 1614, and 1626 nm, and 1419, 1447, and 1467 nm, respectively. It can be seen from Figs. 5(a) and 5(b) that with the increase of d_3 , the red-shift ranges of the resonant wavelengths are smaller than those shown in Figs. 3 and 4, so the changes of the sensing sensitivity are not obvious. In addition,

the *CL* peak value decreases with the increase of d_3 , especially for the analyte RI lower than 1.35. The main reason is considered that the larger d_3 will narrow the leakage channel between the core region and gold film, resulting in the weaker energy coupling from the *x*-pol and *y*-pol core modes to the corresponding second-order SPP modes.

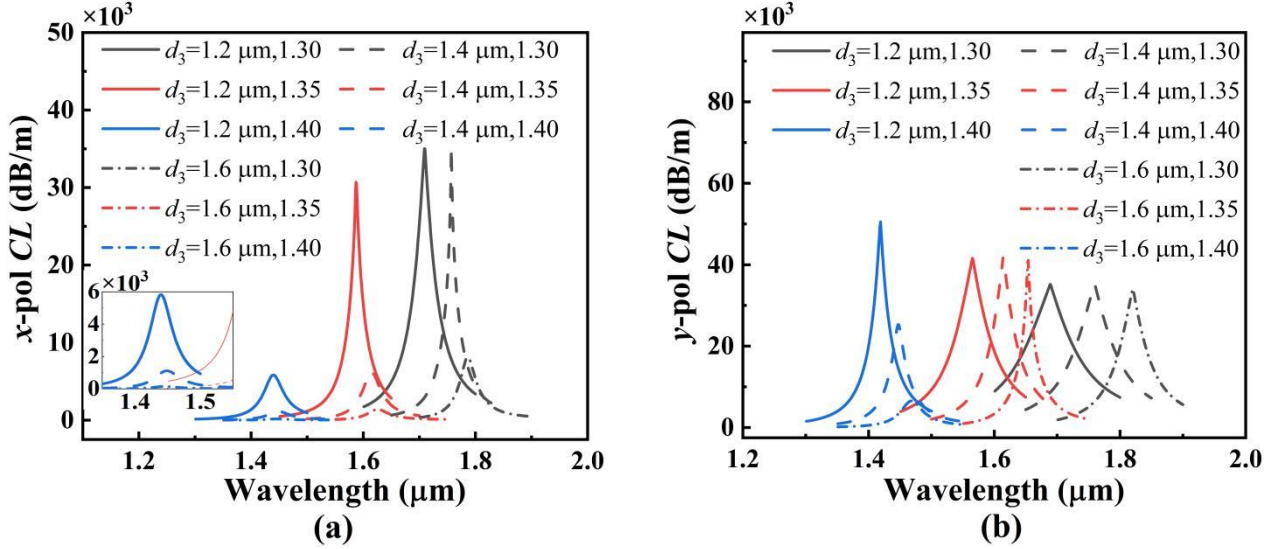


Fig. 5. The *CL* spectra of the *x*-pol (a) and *y*-pol (b) core modes when d_3 is increased from 1.2 to 1.4, and to 1.6 μm and the analyte RI is chosen as 1.30, 1.35, or 1.40, respectively. The insert in (a) shows the zoom-in-spectra of the *x*-pol core mode when d_3 is increased from 1.2 to 1.6 μm and the analyte RI is chosen as 1.40.

Figs. 6(a) and 6(b) show the *CL* spectra of the *x*-pol and *y*-pol core modes of the SPR-PCF when d_4 and the analyte RI are changed. The insert in Fig. 6(a) shows the zoom-in-spectra of the *x*-pol core mode when d_4 is increased from 1.3 to 1.5 μm and the analyte RI is chosen as 1.40. From Fig. 6(a) and the insert, when d_4 is increased from 1.3 to 1.4, and to 1.5 μm and the analyte RI is chosen as 1.30, 1.35, or 1.40, the resonant wavelengths of the *x*-pol core mode are located at 1826, 1757, and 1675 nm, 1659, 1615, and 1552 nm, and 1472, 1449, and 1404 nm, respectively. From Fig. 6(b), when d_4 is increased from 1.3 to 1.4, and to 1.5 μm and the analyte RI is chosen as 1.30, 1.35, or 1.40, the resonant wavelengths of the *y*-pol core mode are located at 1843, 1760, and 1666 nm, 1668, 1614, and 1540 nm, and 1478, 1447, and 1395 nm, respectively. It can be seen from Figs. 6(a) and 6(b) that with the increase of d_4 , the resonant wavelengths of the *x*-pol and *y*-pol core modes occur to blue-shift, and the corresponding sensing sensitivities decrease. In addition for the *x*-pol core mode, the *CL* peak value increases first and then decreases with d_4 for the analyte RI higher than 1.35, while decreases with d_4 for the analyte RI lower than 1.35. For the *y*-pol core mode, the *CL* peak value increases with d_4 for the analyte RI higher than 1.35, while decreases with d_4 for the analyte RI lower than 1.35. The main reason may be that as d_4 is decreased, more energy transfers from the *x*-pol and *y*-pol core modes to the second-order SPP modes and leaks into the cladding region.

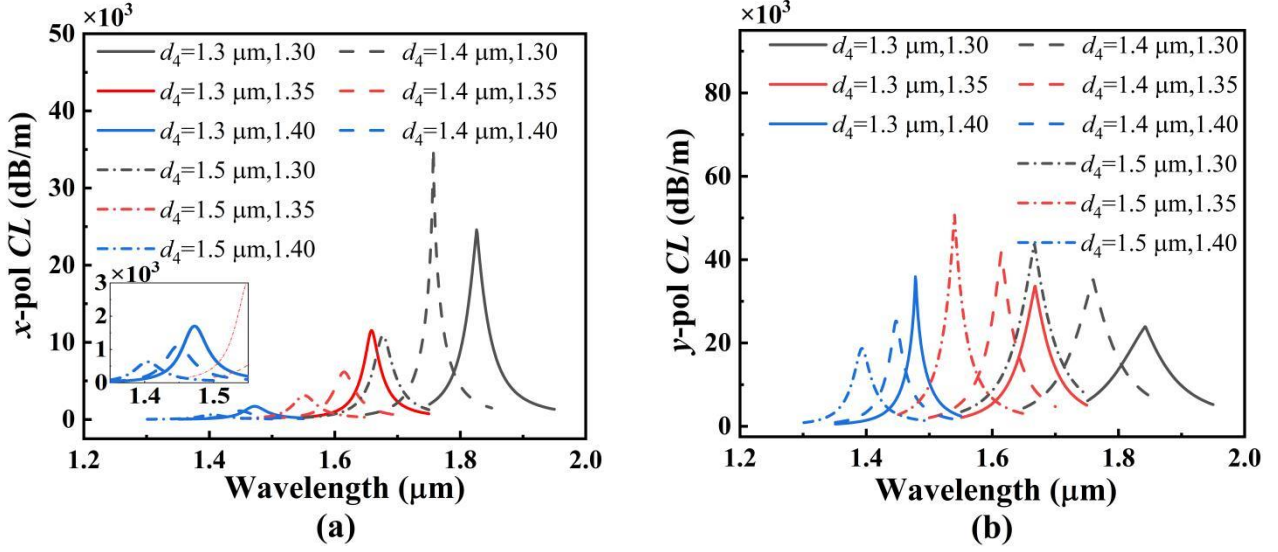


Fig. 6. The *CL* spectra of the *x*-pol (a) and *y*-pol (b) core modes when d_4 is increased from 1.3 to 1.4, and to 1.5 μm and the analyte RI is chosen as 1.30, 1.35, or 1.40, respectively. The insert in (a) shows the zoom-in-spectra of the *x*-pol core mode when d_4 is increased from 1.3 to 1.5 μm and the analyte RI is chosen as 1.40.

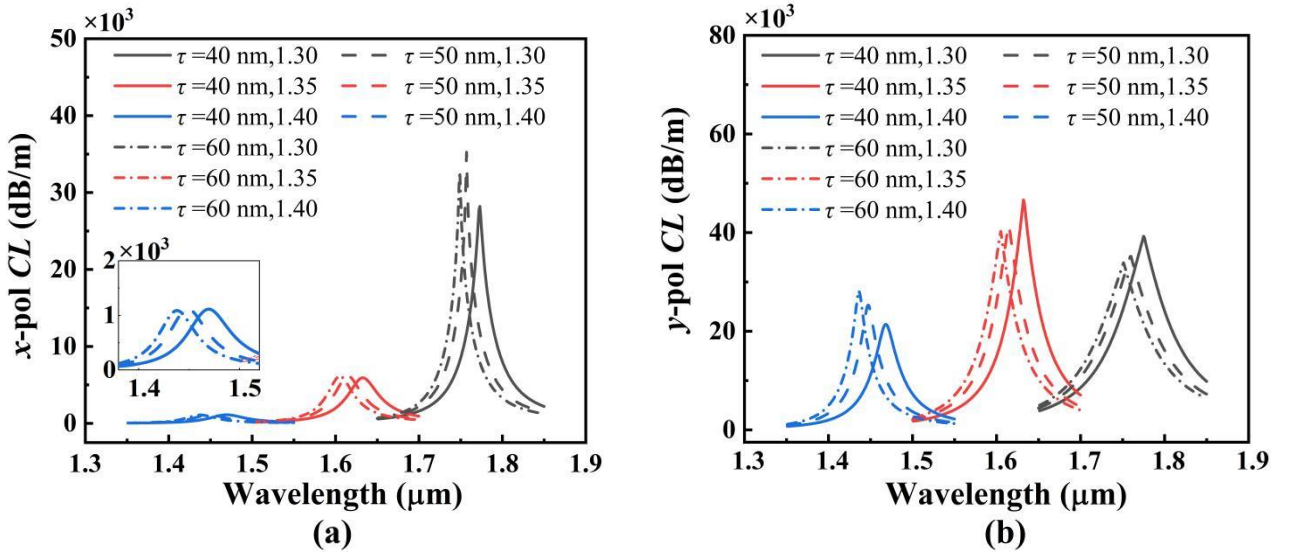


Fig. 7. The *CL* spectra of the *x*-pol (a) and *y*-pol (b) core modes when τ is increased from 40 to 50, and to 60 nm and the analyte RI is chosen as 1.30, 1.35, or 1.40, respectively. The insert in (a) shows the zoom-in-spectra of the *x*-pol core mode when τ is increased from 40 to 60 μm and the analyte RI is chosen as 1.40.

Finally the effect of the gold film thickness τ will be analyzed. Figs. 7(a) and 7(b) show the *CL* spectra of the *x*-pol and *y*-pol core modes of the SPR-PCF when τ and the analyte RI are changed. The insert in Fig. 7(a) shows the zoom-in-spectra of the *x*-pol core mode when τ is increased from 40 to 60 μm and the analyte RI is chosen as 1.40. From Fig. 7(a) and the insert, when τ is increased from 40 to 50, and to 60 nm and the analyte RI is chosen as 1.30, 1.35, or 1.40, the resonant wavelengths of the *x*-pol core mode are located at 1773, 1757, and 1749 nm, 1633, 1615, and 1605 nm, and 1469, 1449, and 1438 nm, respectively. From Fig. 7(b), when τ is increased from 40 to 50, and to 60 nm and the analyte RI is chosen as 1.30, 1.35, or 1.40, the resonant wavelengths of the *y*-pol core mode are located at 1775, 1760, and 1751 nm, 1632, 1614, and 1604 nm, and 1459, 1447, and 1436 nm, respectively. It can be seen from Fig. 7(a) and 7(b) that the resonant wavelengths of

the x -pol and y -pol core modes slightly occur to blue-shift as τ is increased. Thus, τ has little effect on the sensing sensitivities of the x -pol and y -pol core modes. The main reason is due to the slight effect of τ on the SPR effect within the considered wavelength range. In summary the influences of the structure parameter of the proposed SPR-PCF on the propagation characteristics are demonstrated in Table 1.

Table 1. Influences of the structure parameter of the proposed SPR-PCF on the propagation characteristics

Increase of the Structure Parameters	Resonant Wavelength		Wavelength Sensitivity	
	x -pol	y -pol	x -pol	y -pol
d_1	Red-shift	Red-shift	↑	↑
d_2	Red-shift	Red-shift	↑	↑
d_3	Red-shift	Red-shift	↓	↓
d_4	Blue-shift	Blue-shift	↓	↓
τ	Blue-shift	Blue-shift	Unchanged	Unchanged

3. Sensing performances of the proposed SPR-PCF RI sensor

Based on the above analysis, the optimized structure parameters of the proposed SPR-PCF are chosen as following: $d_1=1.8 \mu\text{m}$, $d_2=1.8 \mu\text{m}$, $d_3=1.2 \mu\text{m}$, $d_4=1.4 \mu\text{m}$, $\tau=50 \text{ nm}$, and $\Lambda=2 \mu\text{m}$. In the following, we will investigate the sensing performances of the SPR-PCF RI sensor. Figs. 8(a) and 8(b) show the CL spectra of the x -pol and y -pol core modes when the analyte RI is changed from 1.25 to 1.49. It can be seen from Figs. 8(a) and 8(b) that with the increase of the analyte RI, the CL spectra of the x -pol and y -pol core modes occur to blue-shift, and the corresponding CL peak values increase first and then decrease with the increasing wavelength. The detection boundary is chosen when the CL peak values of the x -pol and y -pol core modes are larger than 1000 dB/m. For the proposed SPR-PCF RI sensor, the ultra-wide RI detection ranges are from 1.25 to 1.45 and from 1.25 to 1.49 for the x -pol and y -pol core modes, respectively.

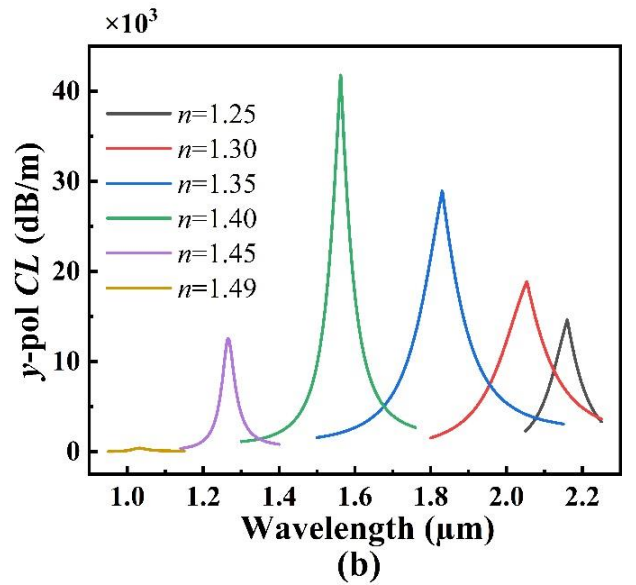
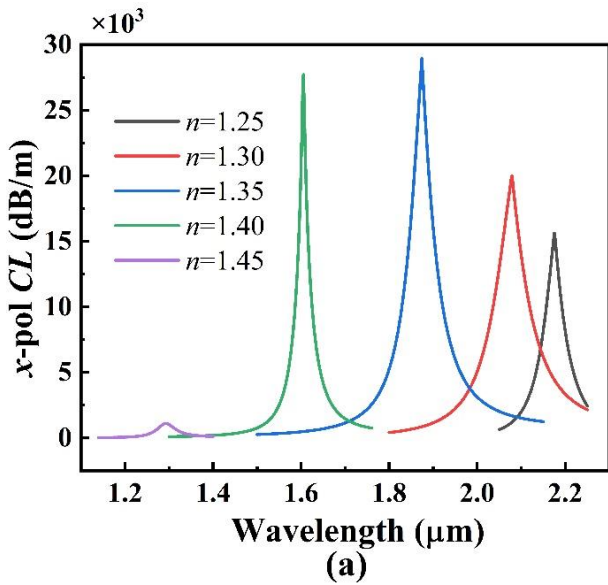


Fig. 8. The CL spectra of the *x*-pol core mode (a) and *y*-pol core mode (b).

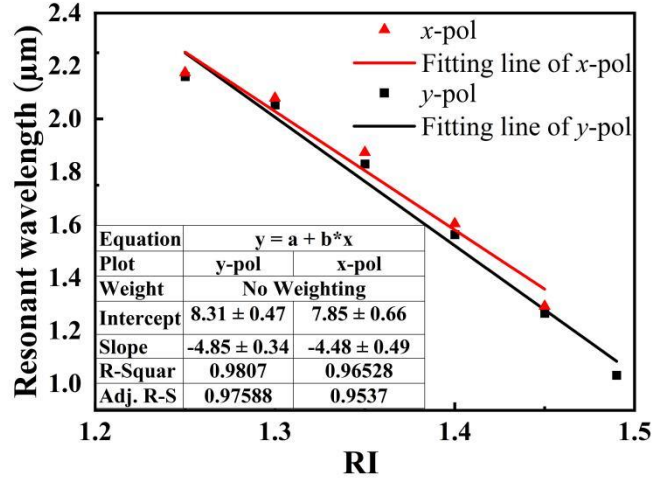


Fig. 9. The linear fitting results of the resonant wavelengths for the *x*-pol and *y*-pol core modes.

Fig. 9 shows the linear fitting results of the resonant wavelengths for the *x*-pol and *y*-pol core modes. As shown in Fig. 9, the linear fitting results of the *x*-pol and *y*-pol core modes are $y = -4.476x + 7.8478$ and $y = -4.85113x + 8.31288$, respectively. And the corresponding R^2 are greater than 0.95 for both *x*-pol and *y*-pol core modes. The RI average sensitivities of the *x*-pol and *y*-pol core modes can achieve -4476.0 nm/RIU and -4851.13 nm/RIU , respectively. Figs. 10(a) and 10(b) show the ASs of the *x*-pol and *y*-pol core modes as functions of wavelength. It can be seen from Figs. 10(a) and 10(b) that the blue-shifts of the resonant wavelengths are noticeable with the increasing RI. The maximum ASs of the *x*-pol and *y*-pol core modes are up to $-1239.19 \text{ RIU}^{-1}$ and $-1633.54 \text{ RIU}^{-1}$, respectively.

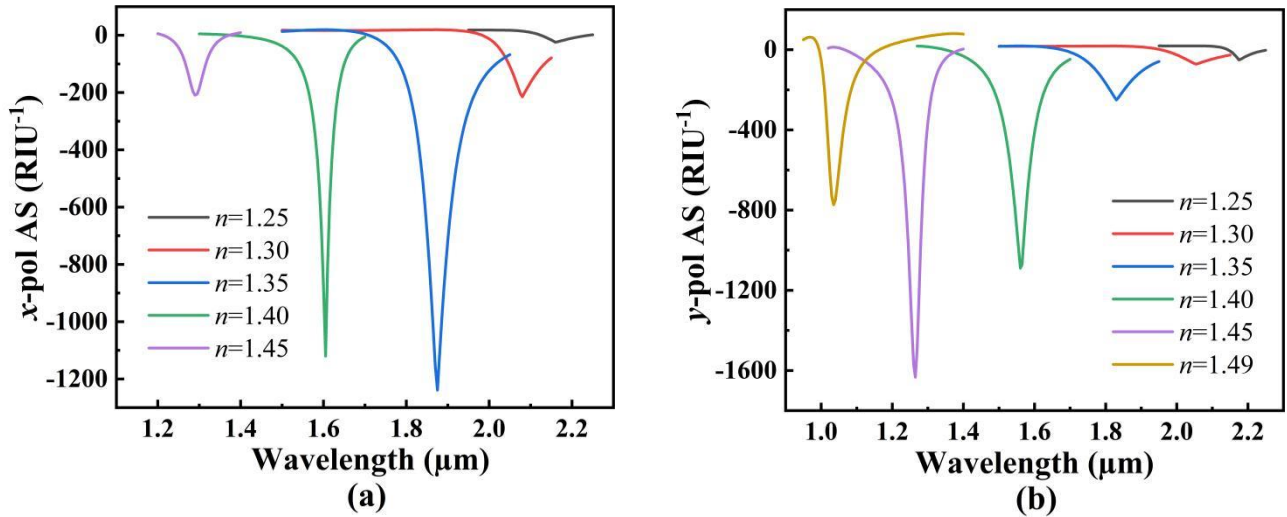


Fig. 10. The ASs of the *x*-pol core mode (a) and *y*-pol core mode (b) as functions of wavelength.

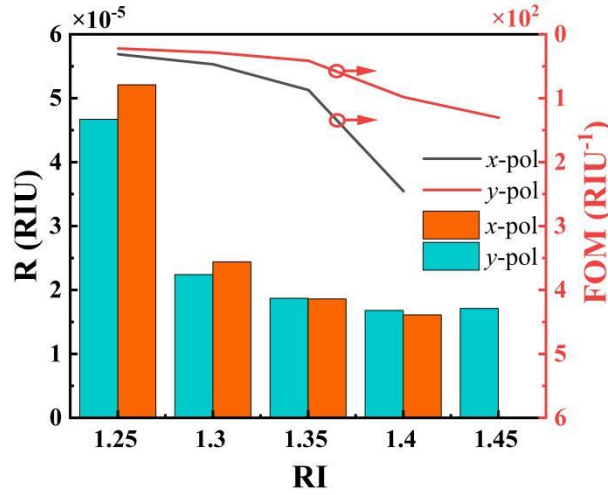


Fig. 11. The changes of the R and FOM with the analyte RI

Fig. 11 shows the changes of the R and FOM with the analyte RI. According to Eqs. (6) and (7), the maximum R values of the x -pol and y -pol core modes are calculated as 1.603×10^{-5} RIU and 1.695×10^{-5} RIU, and the corresponding maximum FOM values are 226.92 RIU⁻¹ and 105.76 RIU⁻¹, respectively. The comparison results of the sensing performances of the proposed SPR-PCF RI sensor with other works are demonstrated in Table 2. It can be seen from the Table 2 that compared with other works, the proposed SPR-PCF RI sensor has the better sensing performances and wider detection range.

Table 2. Comparison results of the RI sensing performances of the proposed SPR-PCF RI sensor with other works.

Refs.	SPR-PCF sensor structures	RI range	WS (nm/RIU)	AS (RIU ⁻¹)	R (RIU)	FOM (RIU ⁻¹)
[15]	Graphene-Silver coated	1.46-1.49	3000	418	2.4×10^{-5}	NA
[16]	Gold-coated spiral	1.33-1.38 (x -pol)	4300	371.5	2.69×10^{-5}	NA
		1.33-1.38 (y -pol)	4600	420.4	2.37×10^{-5}	
[17]	Au nanowires covered	1.33-1.38	4471	214	NA	NA
[18]	Dual optofluidic channel	1.32-1.38	5500	150	1.82×10^{-5}	NA
[19]	Hollow-core graded index optical fiber	1.38-1.49	4350	NA	NA	149
[40]	Graphene-Au coated	1.32-1.41	4200	450	2.3×10^{-5}	NA
This work	Gold-coated	1.25-1.45 (x -pol)	-4476.0	-1239.19	1.603×10^{-5}	226.92
		1.25-1.49 (y -pol)	-4851.13	-1633.54	1.695×10^{-5}	105.76

4. Fabrication and filling processes of the SPR-PCF RI sensor

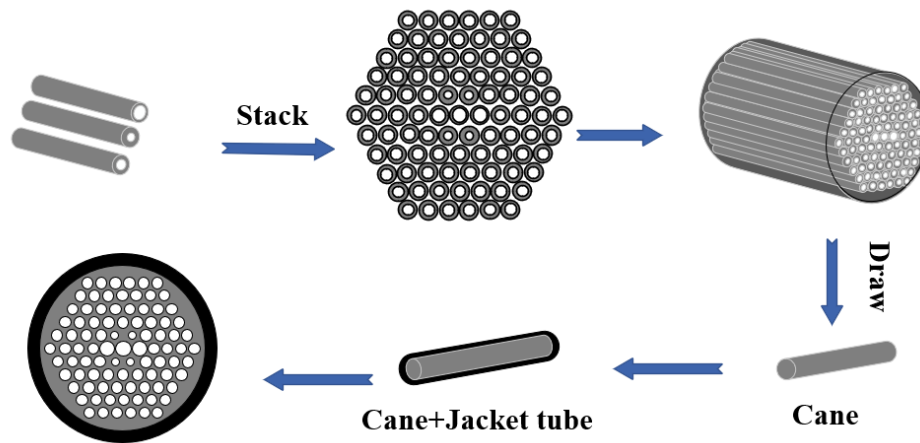


Fig. 12. The schematic diagram of the SPR-PCF fabrication with the stack and draw method.

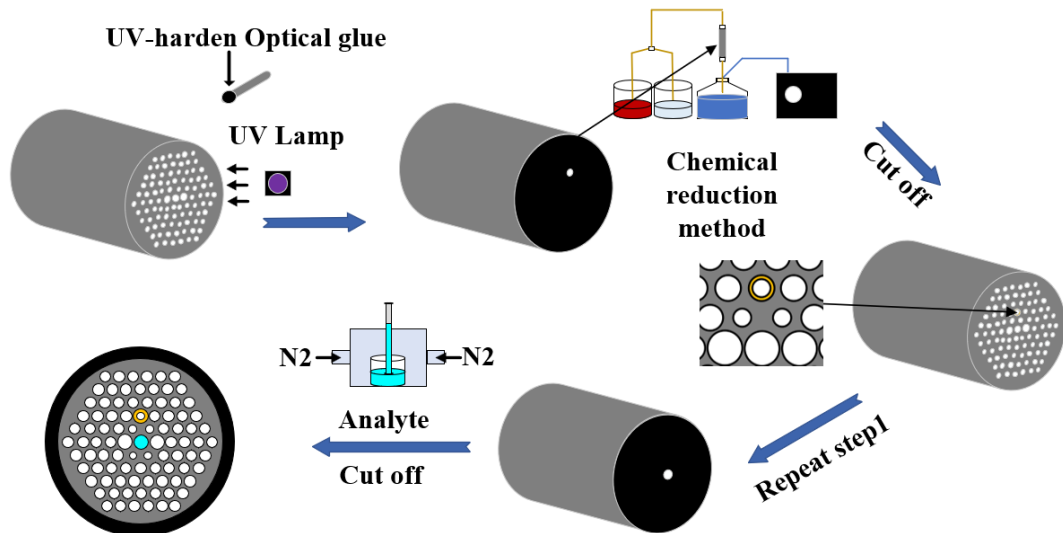


Fig. 13. The schematic diagram of the SPR-PCF coating and filling with the chemical reduction method and selectively filling technique.

It is worth noting that the proposed SPR-PCF RI sensor can be fabricated by using the improved stack and draw method, chemical reduction method and selectively filling technique [41, 42]. Fig. 12 shows the schematic diagram of the SPR-PCF fabrication with the stack and draw method. First, the capillaries with different diameters are stacked in a silica glass tube according to the designed structure. Second, the PCF cane is obtained by drawing the preform under the drawing tower. Finally, the jacket tube is added to the surface of the PCF to obtain the desired PCF.

Fig. 13 shows the schematic diagram of the SPR-PCF coating and filling with the chemical reduction method and selectively filling technique. The gold film of the SPR-PCF coated inside of the air hole can be achieved by the chemical reduction method [43, 44]. First, the air holes which do not need to be coated with the gold film are blocked by the UV glue and illuminated by the UV lamp until the UV glue is solidified. Second, we connect one end of the PCF to a vacuum pump with a silicone tube, and connect the solution containing metal ions to the appropriate reducing agent with a

mixer at the other end. Third, by adjusting the extraction rate of the vacuum chestnut, the gold ions and reducing agent are fully mixed in the mixer, and then pass through the coated air hole of the PCF. The gold particles will be deposited on the air hole and gradually form a gold film. The analyte filling into the air holes can be achieved by the filling technique [45]. Similarly, we use the UV glue to seal the unfilled air hole, insert a section of PCF into analyte, and use a gas pump to fill the analyte into the centre air hole. Finally, the desired length can be obtained by cutting off the SPR-PCF.

5. Conclusion

In conclusion, a novel SPR-PCF RI sensor with ultra-wide detection range is proposed. By introducing the birefringence, the SPR effect is enhanced, and the sensing performances are obviously improved. It is demonstrated that for the *x*-pol and *y*-pol core modes, the average WSs of the SPR-PCF RI sensor are -4476.0 nm/RIU and -4851.13 nm/RIU in the RI range from 1.25 to 1.45 and from 1.25 to 1.49, respectively. The maximum ASs of the SPR-PCF RI sensor can reach -1239.19 RIU⁻¹ and -1633.54 RIU⁻¹ for the *x*-pol and *y*-pol core modes, respectively. Moreover the maximum *R* of 1.603×10^{-5} and 1.695×10^{-5} RIU and *FOM* of 226.92 RIU⁻¹ and 105.76 RIU⁻¹ for *x*-pol and *y*-pol core modes are achieved, respectively. The proposed SPR-PCF RI sensor has potential applications in the chemistry, biology, and environment monitoring.

Acknowledgement

This work is supported by the National Natural Science Foundation of China (Granted No. 61935007).

References

- [1] J. Homola, S. S. Yee, G. Gauglitz, Surface plasmon resonance sensors: review, *Sens. Actuators B Chem.* 54 (1-2) (1999) 3-15.
- [2] Y. Liu, W. Peng, Fiber-optic surface plasmon resonance sensors and biochemical applications: a review, *J. Light. Technol.* 39 (12) (2021) 3781-3791.
- [3] L. G. Carrascosa, A. Ibn Sina, R. Palanisamy, B. Sepulveda, M. A. Otte, Molecular inversion probe-based SPR biosensing for specific, label-free and real-time detection of regional DNA methylation, *Chem. Commun.* 50 (27) (2014) 3585-3588.
- [4] Y. Deng, G. Cao, Y. Wu, X. Zhou, & W. Liao, Theoretical description of dynamic transmission characteristics in MDM waveguide aperture-side-coupled with ring cavity, *Plasmonics* 10(6) (2015) 1537-1543.
- [5] F. Zhao, J. Lin, Z. Lei, Z. Yi, F. Qin, J. Zhang, P. Wu, Realization of 18.97% theoretical efficiency of 0.9 μm thick c-Si/ZnO heterojunction ultrathin-film solar cells via surface plasmon resonance enhancement, *Phys. Chem. Chem. Phys.* 24(8) (2022) 4871-4880.
- [6] Z. Zheng, Y. Zheng, Y. Luo, Z. Yi, J. Zhang, Z. Liu, P. Wu, A switchable terahertz device combining ultra-wideband absorption and ultra-wideband complete reflection, *Phys. Chem. Chem. Phys.* 24(4) (2022) 2527-2533.
- [7] F. Zhou, F. Qin, Z. Yi, W. Yao, Z. Liu, X. Wu, P. Wu, Ultra-wideband and wide-angle perfect solar energy absorber based on Ti nanorings surface plasmon resonance. *Phys. Chem. Chem. Phys.* 23(31) (2021) 17041-17048.
- [8] Y. Deng, G. T. Cao, H. Yang, X. Q. Zhou, Y. W. Wu, Dynamic control of double plasmon-induced transparencies in aperture-coupled waveguide-cavity system, *Plasmonics* 13(1) (2018) 345-352.

- [9] D. Hu, H. P. Ho, Recent advances in plasmonic photonic crystal fibers: design, fabrication and applications, *Adv. Opt. Photonics* 9 (2) (2017) 257-314.
- [10] J. Homola, Present and future of surface plasmon resonance biosensors, *Anal. Bioanal. Chem.* 377 (3) (2003) 528-539.
- [11] A. G. Brolo, Plasmonics for future biosensors, *Nat. Photonics* 6 (11) (2012) 709-713.
- [12] Z. K. Fan, S. G. Li, Q. Liu, G. W. An, H. L. Chen, J. S. Li, W. L. Tian, High sensitivity of refractive index sensor based on analyte-filled photonic crystal fiber with surface plasmon resonance, *IEEE Photon. J.* 7 (3) (2015) 1-9.
- [13] H. L. Chen, S. G. Li, J. S. Li, Z. K. Fan, Magnetic field sensor based on magnetic fluid selectively infilling photonic crystal fibers, *IEEE Photon. Technol. Lett.* 27 (7) (2015) 717-720.
- [14] A. Hassani, M. Skorobogatiy, Design of the microstructured optical fiber-based surface plasmon resonance sensors with enhanced microfluidics, *Opt. Express* 14 (24) (2006) 11616-11621.
- [15] A. A. Rifat, G. A. Mahdiraji, D. M. Chow, Y. G. Shee, R. Ahmed, F. R. M. Adikan, Photonic crystal fiber-based surface plasmon resonance sensor with selective analyte channels and graphene-silver deposited core, *Sensors* 15 (5) (2015) 11499-11510.
- [16] M. R. Hasan, S. Akter, A. A. Rifat, S. Rana, K. Ahmed, R. Ahmed, D. Abbott, Spiral photonic crystal fiber-based dual-polarized surface plasmon resonance biosensor, *IEEE Sens. J.* 18 (1) (2018) 133-140.
- [17] A. K. Pathak, B. M. A. Rahman, V. K. Singh, S. Kumari, Sensitivity enhancement of a concave shaped optical fiber refractive index sensor covered with multiple Au nanowires, *Sensors* 19 (19) (2019) 4210.
- [18] N. Chen, M. Chang, X. L. Lu, J. Zhou, X. D. Zhang, Photonic crystal fiber plasmonic sensor based on dual optofluidic channel, *Sensors* 19(23) (2019) 5150.
- [19] R. Nasirifar, M. Danaie, A. Dideban, Hollow-core graded index optical fiber refractive index sensor based on surface plasmon resonance, *Opt Quantum Electron* 52(7) (2020) 341.
- [20] G. Y. Wang, Y. Lu, L. C. Duan, J. Q. Yao, A refractive index sensor based on PCF with ultra-wide detection range, *IEEE J Quantum Electron* 27 (4) (2021) 1-8.
- [21] X. Y. Liu, G. Melwin, M. S. A. Gandhi, H. Y. Fu, P. R. Babu, K. Senthilnathan, Q. Li, Ultrahigh sensitive surface plasmon sensor using a nanofilm coated D-type photonic crystal fiber, *Appl. Opt.* 60 (9) (2021) 2591-2598.
- [22] M. T. De, V. K. Singh, Wide range refractive index sensor using a birefringent optical fiber, *Opt Quantum Electron* 53 198 (2021).
- [23] X. Yu, Y. Zhang, S. S. Pan, P. Shum, M. Yan, Y. Leviatan, C. M. Li, A selectively coated photonic crystal fiber based surface plasmon resonance sensor, *J Opt* 12 (1) (2010).
- [24] Y. Du, S. G. Li, S. Liu, Wavelength-selective characteristics of high birefringence photonic crystal fiber with Au nanowires selectively filled in the cladding air holes, *Chin. Phys. B* 21 (9) (2012).
- [25] E. Haque, M. A. Hossain, Y. Namihira, F. Ahmed, Microchannel-based plasmonic refractive index sensor for low refractive index detection, *Appl. Opt.* 58 (6) (2019) 1547-1554.
- [26] Y. Qu, J. H. Yuan, X. Zhou, F. Li, C. Mei, B. B. Yan, C. X. Yu, A V-shape photonic crystal fiber polarization filter based on surface plasmon resonance effect, *Opt. Commun.* 452 (2019) 1-6.
- [27] S. Qiu, J. H. Yuan, X. Zhou, F. Li, Q. W. Wang, Y. W. Qu, C. X. Yu, Hollow-core negative curvature fiber with high birefringence for low refractive index sensing based on surface plasmon resonance effect, *Sensors* 20 (22) (2020) 6539.
- [28] X. C. Yang, Y. Lu, B. L. Liu, J. Q. Yao, Polarization characteristics of high-birefringence photonic crystal fiber selectively coated with silver layers, *Plasmonics* 13 (3) (2018) 1035-1042.
- [29] A. A. Rifat, F. Haider, R. Ahmed, G. A. Mahdiraji, F. R. M. Adikan, A. E. Miroshnichenko, Highly sensitive selectively coated photonic crystal fiber-based plasmonic sensor, *Opt. Lett.* 43 (4) (2018) 891-894.

- [30] C. Liu, L. Yang, X. L. Lu, Q. Liu, F. M. Wang, J. W. Lv, P. K. Chu, Mid-infrared surface plasmon resonance sensor based on photonic crystal fibers, *Opt. Express* 25 (13) (2017) 14227-14237.
- [31] T. S. Li, L. Q. Zhu, X. C. Yang, X. P. Lou, L. D. Yu, A refractive index sensor based on H-shaped photonic crystal fibers coated with Ag-Graphene layers, *Sensors* 20 (3) (2020) 741.
- [32] S. X. Jiao, S. F. Gu, H. R. Fang, H. R. Yang, Analysis of dual-core photonic crystal fiber based on surface plasmon resonance sensor with segmented silver film, *Plasmonics* 14 (3) (2019) 685-693.
- [33] X. Wu, Y. Zheng, Y. Luo, J. Zhang, Z. Yi, X. Wu, P. Wu, A four-band and polarization-independent BDS-based tunable absorber with high refractive index sensitivity, *Phys. Chem. Chem. Phys.* 23(47) (2021) 26864-26873.
- [34] C. Liu, J. W. Wang, F. M. Wang, W. Q. Su, Q. Liu, Surface plasmon resonance (SPR) infrared sensor based on D-shape photonic crystal fibers with ITO coatings, *Opt. Commun.* 464 (2020) 125496.
- [35] S. D. Chu, K. Nakkeeran, A. M. Abobaker, S. S. Aphale, P. R. Babu, K. Senthilnathan, Design and analysis of surface-plasmon-resonance-based photonic quasi-crystal fiber biosensor for high-refractive-index liquid analytes, *IEEE J Quantum Electron* 25 (2) (2019) 1-9.
- [36] G. W. An, S. G. Li, X. Yan, Z. Y. Yuan, X. N. Zhang, High-birefringence photonic crystal fiber polarization filter based on surface plasmon resonance, *Appl. Opt.* 55 (6) (2016) 1262-1266.
- [37] C. Jocher, C. Jauregui, C. Voigtlander, F. Stutzki, S. Nolte, J. Limpert, A. Tunnermann, Fiber based polarization filter for radially and azimuthally polarized light, *Opt. Express* 19 (20) (2011) 19582-19590.
- [38] M. I. A. Isti, H. Talukder, S. M. R. Islam, S. Nuzhat, A. S. M. S. Hosen, G. H. Cho, S. K. Biswas, Asymmetrical D-channel photonic crystal fiber-based plasmonic sensor using the wavelength interrogation and lower birefringence peak method, *Results in Phys.* 19 (2020) 103372.
- [39] Y. Huang, Y. Wang, L. Zhang, Y. Shao, F. Zhang, C. Liao, Y. Wang, Tunable electro-optical modulator based on a photonic crystal fiber selectively filled with liquid crystal, *J. Light. Technol.* 37 (9) (2019) 1903-1908.
- [40] H. Y. Yang, M. Y. Liu, Y. P. Chen, L. Guo, G. L. Xiao, H. Q. Liu, L. B. Yuan, Highly sensitive Graphene-Au coated plasmon resonance PCF sensor, *Sensors* 21 (3) (2021) 818.
- [41] B. B. Shuai, L. Xia, D. M. Liu, Coexistence of positive and negative refractive index sensitivity in the liquid-core photonic crystal fiber based plasmonic sensor, *Opt. Express* 20 (23) (2012) 25858-25866.
- [42] H. W. Lee, M. A. Schmidt, R. F. Russell, N. Y. Joly, H. K. Tyagi, P. Uebel, P. S. J. Russell, Pressure-assisted melt-filling and optical characterization of Au nano-wires in microstructured fibers, *Opt. Express* 19 2011 12180-12189.
- [43] M. D. Lu, W. Peng, Q. Liu, Y. Liu, L. X. Li, Y. Z. Liang, J. F. Masson, Dual channel multilayer-coated surface plasmon resonance sensor for dual refractive index range measurements, *Opt. Express* 25(8) (2017) 8563-8570.
- [44] Y. W. Shi, K. Ito, L. Ma, T. Yoshida, Y. Matsuura, and M. Miyagi, Fabrication of a polymer-coated silver hollow optical fiber with high performance, *Appl. Opt.* 45(26) (2006) 6736-6740.
- [45] Q. Liu, S. Li, X. Gao, Highly sensitive plasmonics temperature sensor based on photonic crystal fiber with a liquid core, *Opt. Commun.* 427 (2018) 622-627.